

12,05

## Influence of functionalization with citric acid on the properties of magnetic nanoparticles $Zn_xFe_{3-x}O_4$ ( $0 \leq x \leq 1.0$ )

© A.S. Kamzin<sup>1</sup>, G. Caliskan<sup>2</sup>, N. Dogan<sup>2</sup>, A. Bingolbali<sup>3</sup>, V.G. Semenov<sup>4</sup>, I.V. Buryanenko<sup>5</sup>

<sup>1</sup> Ioffe Institute,  
St. Petersburg, Russia

<sup>2</sup> Department of Physics, Gebze Technical University,  
Kocaeli, Turkey

<sup>3</sup> Department of Bioengineering, Yıldız Technical University,  
Istanbul, Turkey

<sup>4</sup> St. Petersburg State University,  
St. Petersburg, Russia

<sup>5</sup> Peter the Great Saint-Petersburg Polytechnic University,  
St. Petersburg, Russia

E-mail: ASKam@mail.ioffe.ru

Received May 29, 2022

Revised May 29, 2022

Accepted May 30, 2022

The effect of surface functionalization with citric acid on the properties of magnetic nanoparticles (MNPs)  $Zn_xFe_{3-x}O_4$  ( $x = 0; 0.25; 0.5; 0.75; 1.0$ ) synthesized by the hydrothermal method was studied. To study the properties of MNPs, X-ray diffractometry (XRD) and energy dispersive X-ray spectroscopy (EDS) were used. The magnetic properties of the samples and the phase state of MNPs were studied using a physical property measurement system (PPMS) and Mössbauer spectroscopy (MS). It has been established that the sizes of crystallites and the crystal lattice parameter of  $Zn_xFe_{3-x}O_4$  MNPs change with increasing  $Zn^{2+}$  concentration. The low values of the coercive force and the presence of a doublet on the MS indicate the presence of both ferrimagnetic and superparamagnetic components.

**Keywords:**  $Zn_xFe_{3-x}O_4$  ferrite spinel MNPs, hydrothermal synthesis, functionalization of MNPs with citric acid, crystal structure, magnetic properties, magnetic structure.

DOI: 10.21883/PSS.2022.10.54249.391

### 1. Introduction

The uniqueness of the properties of magnetic nanoparticles (MNPs), which differ significantly from their bulk analogues, attracts great interest of researchers both from the point of view of fundamental studies of the properties of MNPs [1–4], and practical applications (see for example [5] and references there), including use in various fields of biomedicine, such as to enhance the contrast of magnetic resonance imaging (MRI), for drug delivery, nanoprobes for imaging *in-vivo*, treatment of magnetic hyperthermia, etc. [6–10]. The MNPs required for biomedicine should have high values of magnetization, a narrow particle size distribution and, most importantly, have biological compatibility. To produce such materials, MNPs of magnetite ( $Fe_3O_4$ ) doped with transition metals such as zinc ( $Zn^{2+}$ ), nickel ( $Ni^{2+}$ ), manganese ( $Mn^{2+}$ ) and copper ( $Cu^{2+}$ ) are intensively studied [11–14].

The structural properties, size, morphology, surface condition and chemical homogeneity of the MNPs depend on the synthesis method. To obtain the required MNPs and controlled synthesis of particles with specified magnetic properties, various methods are used: co-deposition, hydrothermal synthesis, microwave com-

bustion, sol-gel-spontaneous combustion, spray pyrolysis, etc. [15–23].

However, the introduction of MNPs into a living organism is unacceptable for a number of reasons. First, human physiological environments (blood, etc.) biochemically easily recognize viruses, bacteria, etc., as well as foreign materials, which are then passivated by the immune system. In addition, synthesized MNPs can be toxic and not biologically compatible. In connection with these requirements, hybrid MNPs of the core/shell type are created, the protective shell of which is silicon dioxide [24] or biologically compatible iron oxides [25,26]. Secondly, magnetic liquids (ML), developed for introduction into a living organism, are a mixture of MNPs dispersed into an aqueous medium or other liquids. In this case, MNPs with stability of properties in the liquid, demonstrating and maintaining the proper state of dispersion under specified physico-chemical conditions are required. To do this, the chemical composition of the surface of the particles is modified (functionalized) and hybrid colloidal MNPs (HCMNPs) are formed, which make it possible to obtain homogeneous ML with high colloidal stability, biocompatibility and lack of toxicity. Functionalization changes the properties inherent in the surface of MNPs.

Various coating materials are used to create HCMNPs, including citric [27,28], ascorbic [29], tartaric [30] acids, dextran [31], graphene oxide [32–34] and others [35–39]. Accordingly, citric acid (CA) can be adsorbed on the surface of iron oxide nanoparticles [40]. Among the various small molecules, citric acid ( $C_6H_8O_7$ ), a biocompatible short-chain tricarboxylic acid, is used to prepare water-stable iron oxide nanoparticles for biomedical applications [41]. The CA coating also prevents agglomeration of the MNPs and makes the surface of the nanoparticles hydrophilic.

With their unique multifunctional synergetic characteristics, colloidal hybrids (HCMNPs) have attracted considerable research interest, as they represent a new and breakthrough application in a wide variety of fields, including biomedicine [28–32,36,38,39]. However, despite the large number of works on the synthesis of HCMNPs, the experimental data obtained on the influence of different coatings on the magnetic properties of the MNPs are far from sufficient, and the available ones are quite contradictory.

This paper investigates the properties of magnetite MNPs depending on the concentration of substitute ions  $Zn^{2+}$  ( $Zn_xFe_{3-x}O_4$  at  $x = 0, 0.25, 0.5, 0.75, 1$ ). The unusual magnetic properties of the ferrites  $Zn_xFe_{3-x}O_4$  attracts researchers to their studies, including for biomedical applications [14,40–43]. In the reference [40] a quantitative analysis of the dependence of the specific absorption rate of the nanoparticles  $Zn_xFe_{3-x}O_4$  ( $0 \leq x \leq 0.5$ ) with dimensions of 16 nm on the strength of the applied magnetic field was carried out and it was established that the specific absorption rate increases to  $x = 0.3$ , and then decreases. Even a small amount of Zn ions introduced into magnetite can significantly increase the saturation magnetization of the MNPs  $Zn_xFe_{3-x}O_4$  [44,45]. Ferrimagnetic properties can be observed in the MNPs of zinc ferrite at temperatures well above the magnetic ordering point ( $\sim 10.5$  K). The choice of ions  $Zn^{2+}$  for doping magnetite is justified by the fact that ions Zn are characterized by the absence of toxicity.

Another task was to study the effect of CA coverage (functionalization) on the properties of the MNPs  $Zn_xFe_{3-x}O_4$ . Therefore, MNPs  $Zn_xFe_{3-x}O_4$ , functionalized CA ( $Zn_xFe_{3-x}O_4@CA$ ) were also synthesized and comparative studies of the properties of the obtained MNPs were carried out. The choice of CA for the functionalization of MNPs  $Zn_xFe_{3-x}O_4$  is based on the fact that CA has unique qualities such as biocompatibility, non-toxicity and solubility in water.

For the synthesis of the studied MNPs  $Zn_xFe_{3-x}O_4$ , a hydrothermal method was used. The method was first developed in 1845 and is a simple, cost-effective and environmentally friendly method [46,47]. However, the magnetite MNPs synthesized by the hydrothermal method usually had rounded, but rather fuzzy shapes; therefore, it is necessary to modify the hydrothermal synthesis method in order to obtain quasi-spherical MNPs of given sizes.

The novelty of this study lies in the study of changes in the crystal structure and magnetic properties of magnetite MNPs during doping with zinc ( $Zn_xFe_{3-x}O_4$ ), as well as

during the functionalization of the surface of the MNPs  $Zn_xFe_{3-x}O_4$  with citric acid. Another objective of this work was to modify the hydrothermal synthesis method to produce the MNPs  $Zn_xFe_{3-x}O_4@CA$  with high magnetic characteristics and small dispersion in size required for biomedical applications.

## 2. Experimental methods

### 2.1. Synthesis of MNPs $Zn_xFe_{3-x}O_4$ ( $x = 0, 0.25, 0.5, 0.75, 1.0$ )

For the synthesis of MNPs  $Zn_xFe_{3-x}O_4$ , at  $x = 0, 0.25, 0.5, 0.75, 1.0$ , iron chloride tetrahydrate ( $FeCl_2 \cdot 4H_2O$ ), iron chloride hexahydrate ( $FeCl_3 \cdot 6H_2O$ ), zinc chloride ( $ZnCl_2$ ) and ammonium hydroxide ( $NH_4OH$ , 25% ammonia) were used from Sigma Aldrich with a minimum purity of 99%.

$Zn_xFe_{3-x}O_4$  (at  $x = 0, 0.25, 0.5, 0.75, 1.0$ ) particles are synthesized hydrothermally. The precursor for the production of  $Zn_xFe_{3-x}O_4$  nanoparticles consisted of 4 mMol salts  $FeCl_3 \cdot 6H_2O$ ,  $FeCl_2 \cdot 4H_2O$  and  $ZnCl_2$ , dissolved in 40 ml distilled water. Then, 5 ml of 25% aqueous solution of  $NH_4OH$  was added to the solution. The resulting solution was stirred with a mechanical stirrer at 500 rpm at room temperature for 2 min in a nitrogen atmosphere. The solution was placed in a Teflon seal autoclave and kept at 180°C for 12 hours. The autoclave was then naturally cooled and the resulting precipitate was washed three times with distilled water and separated with a magnet. Analysis of the resulting powder showed that these are particles of ferrite  $Zn_xFe_{3-x}O_4$ .

For functionalization with citric acid, the resulting  $Zn_xFe_{3-x}O_4$  particles were mixed with 50 ml of deionized water and 3 mMol of citric acid. The resulting solution was stirred in an ultrasonic bath at 65°C. Then, 1 ml of an aqueous solution of  $NH_4OH$  was added to the mixture and mechanically stirred for 30 min in a nitrogen atmosphere. The final products of black color were then washed with deionized water and dried at 60°C for 2 h and were ready to study their characteristics.

### 2.2. Research methods of MNPs $Zn_xFe_{3-x}O_4$

The structures of the lattices of the synthesized MNPs were determined using the X-ray diffractometer (XRD) Rigaku 2200 with  $CuK\alpha$ -radiation with wavelength  $\lambda = 0.154$  nm (at 40 kV and 35 mA) in the range of diffraction angles from 10° to 90° ( $2\theta$ ) with scanning pitch of 0.02°. The magnetic hysteresis loops of these samples were measured using the Quantum Design Model 6000 physical property measurement system (PPMS). The magnetic properties of the nanoparticles, namely the saturation magnetization  $M_s$ , the coercive field  $H_c$  and the residual magnetization  $M_r$ , were derived from the loops of magnetic hysteresis.

The magnetic properties and phase state of the synthesized MNPs were investigated using Mössbauer spectroscopy, which has a high sensitivity to nuclear ultrafine

interactions and allows unambiguous identification of iron oxides [14,25,26,33,34,48–50], which is not available to other methods. Mössbauer spectra (MS) of the synthesized MNPs were obtained using a spectrometer with registration of gamma-quanta from the source  $\text{Co}^{57}(\text{Rh})$  in the geometry of transmission through the sample. The speed scale is calibrated using foil  $\alpha\text{-Fe}$  with thickness of  $6\ \mu\text{m}$  at room temperature. Mathematically experimental MS were processed using a specialized program [51], which describes the spectral lines by peaks of the Lorentz shape by the method of least squares. The complexity of the analysis required a procedure for reconstructing the probabilities of the distribution of effective magnetic fields  $H_{\text{eff}}$  from experimental MS using the program [51]. The discrepancy between the theoretical values of the parameters of ultrafine interactions (UFIs) is determined by statistical deviations. In the procedure of minimizing the functionality  $\chi^2$ , the program searches for optimal values of parameters, namely the width, intensity and position of spectral lines. Using the positions of the spectral lines on the speed scale, the UFI parameters are calculated: IS — isomeric shift of Mössbauer lines, QS — quadrupole splitting,  $H_{\text{eff}}$  — effective magnetic field.

### 3. Experimental results and analysis

#### 3.1. Results of XRD studies

The crystal structure and phase identification of the magnetic nanoparticles were established using the X-ray diffraction (XRD) performed on powder samples. Figure 1 shows the X-ray diffraction pattern of the samples. The position and relative intensities of all diffraction peaks can be attributed to the crystallographic planes (220), (311), (222), (400), (422), (511) and (440), corresponding to the cubic crystal structure of the magnetite spinel, which correspond to the JCPDS map № 00-019-0629 [52]. In the sample  $\text{Zn}_{0.75}\text{Fe}_{2.25}\text{O}_4@CA$  an impurity phase of hematite ( $\alpha\text{-Fe}_2\text{O}_3$ ) was detected. A comparison of the XRD data of  $\text{Zn}_{0.75}\text{Fe}_{2.5}\text{O}_4$  and  $\text{Zn}_{0.75}\text{Fe}_{2.25}\text{O}_4@CA$  MNPs showed that the effect of citric acid covering the MNPs on the crystal structure of  $\text{Zn}_x\text{Fe}_{3-x}\text{O}_4$  particles is absent. The severity of the XRD peaks in the case of  $\text{Zn}_{0.75}\text{Fe}_{2.25}\text{O}_4@CA$  indicates a higher-order crystallinity than other samples.

The average crystallite sizes  $D$  (nm) are calculated using the Debye–Scherrer equation [53] and the line of maximum intensity (311). The results of the calculations are shown in Fig. 2, which shows that the particle size increases with the doping of magnetite with Zn, with the exception of samples  $\text{Zn}_{0.25}\text{Fe}_{2.75}\text{O}_4@CA$  and  $\text{ZnFe}_2\text{O}_4@CA$ .

The lattice parameters  $\alpha$  of the samples were calculated using the equation (1):

$$\alpha = d_{hkl} \sqrt{h^2 + k^2 + l^2}, \quad (1)$$

where  $d_{hkl}$  — the interplane distance describing the distance between the planes of atoms,  $hkl$  — Miller indices. The

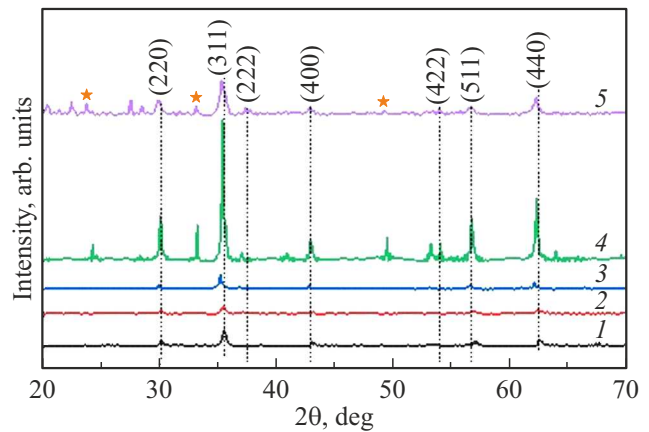


**Figure 1.** X-ray diffractograms of  $\text{Zn}_x\text{Fe}_{3-x}\text{O}_4@CA$  nanoparticles, at  $x = 0, 0.25, 0.5, 0.75$  and  $1.0$ , designated 1, 2, 3, 4 and 5, respectively. Lines belonging to  $\text{Fe}_2\text{O}_3$  are marked with an asterisk (\*).

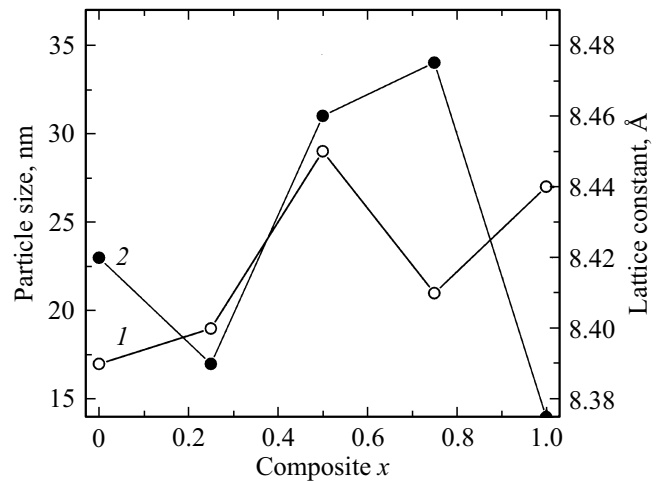


**Figure 2.** Particle sizes (curve 1) and crystal lattice parameters (curve 2) of MNPs  $\text{Zn}_x\text{Fe}_{3-x}\text{O}_4@CA$  depending on the number of ions Zn, calculated from X-ray diffractogram data.

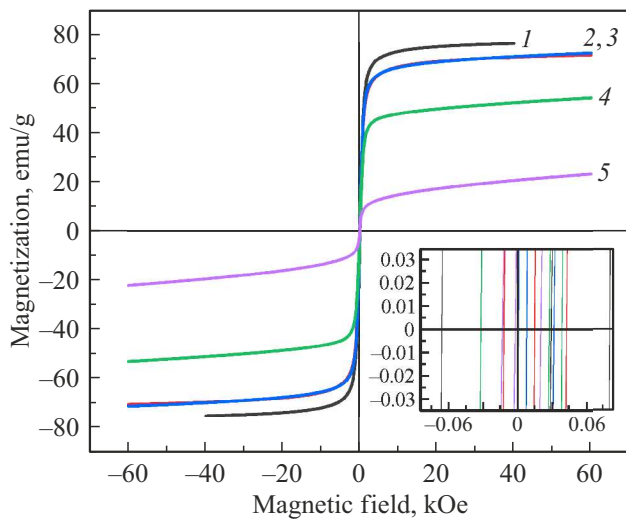
average value of  $\alpha$  for the MNPs of magnetite was equal to  $8.418\ \text{\AA}$ , which is close to the value of bulk magnetite ( $8.396\ \text{\AA}$ ), and not maghemite ( $8.3315\ \text{\AA}$ ) [32]. The largest value of the lattice parameter in  $\text{Zn}_{0.75}\text{Fe}_{2.25}\text{O}_4@CA$  indicates that the sample is a mixture of normal and inverse structures. As can be seen in Fig. 2, the lattice parameter increases when Zn is doped, and then decreases, which seems to be due to the distribution of the cations  $\text{Zn}^{2+}$  and  $\text{Fe}^{3+}$  in the internodes.

#### 3.2. Results of studies of magnetic properties

Magnetization changes in the magnetic field  $M(H)$  of  $\text{Zn}_x\text{Fe}_{3-x}\text{O}_4@CA$  samples obtained using PPMS in the range of the external magnetic field from  $-60\ \text{kOe}$  to  $+40\text{--}6\ \text{Oe}$  are shown in Fig. 3.

**Table 1.** Magnetic characteristics of MNPs  $Zn_xFe_{3-x}O_4@CA$  at 300 K

Sample	$M_s$ , emu/g	$M_r$ , emu/g	$H_c$ , Oe	SQR ( $M_r/M_s$ )	$K$ , J/m <sup>3</sup>	$n_B, \mu_B$
$Fe_3O_4@CA$	40	0.46	15	0.011	937.5	1.65
$Zn_{0.25}Fe_{2.75}O_4@CA$	60	0.01	28	0	2700	2.51
$Zn_{0.5}Fe_{2.5}O_4@CA$	60	0	24	0	2250	2.53
$Zn_{0.75}Fe_{2.25}O_4@CA$	60	0	41	0	3843	2.56
$ZnFe_2O_4@CA$	60.01	0	28	0	2625	2.59

**Figure 3.** Hysteresis loops of nanoparticles  $Zn_xFe_{3-x}O_4@CA$ . The numbers 1, 2, 3, 4 and 5 indicate the concentrations of Zn ( $x$ ) in samples 0, 0.25, 0.5, 0.75, 1.0, respectively.

MNPs  $Zn_xFe_{3-x}O_4$ , as well as coated with CA MNPs  $Zn_xFe_{3-x}O_4@CA$  demonstrate at 300 K a nonlinear dependence of magnetization on a magnetic field. Table 1 shows that the saturation magnetization of  $M_s$  increases from 40 emu/g to 60.01 emu/g with an increase in substitution with ions Zn from 0 to 1.

The residual magnetizations of the  $M_r$  of the samples are negligible, and the coerciveness of the  $H_c$  varies between 15–41 Oe. This indicates the homogeneity of the studied particles that are in the superparamagnetic phase. Particle sizes  $Zn_{0.75}Fe_{2.25}O_4@CA$ , as shown in Fig. 2, is larger than other samples, which may cause the high coerciveness of these particles at 300 K.

The hysteresis loop rectangularity ratio (SQR) shows the ratio of the residual magnetization values  $M_r$  to the saturation magnetization values of  $M_s$ . The SQR values correspond to the superparamagnetic behavior of the particles behavior of the particles studied. The theoretical limits of 0.50 and 0.83 define a unidomain structure with uniaxial and cubic anisotropy according to Stoner–Wohlfarth theory [54]. The obtained SQR values were less than 0.5, which may be due to the effects of surface spin disorder.

#### 4. Mössbauer spectrometry of MNPs of ferrites

The main advantages of Mössbauer spectroscopy are that this method allows you to confidently establish the phase composition, the distribution of ions in non-equivalent positions, the magnetic structure, the percentage of compounds with iron and ultrafine interactions in iron-containing materials [24–26,33,34,48–50]. This is due to the possibilities of Mössbauer spectroscopy for the unambiguous identification of iron oxides, which is practically inaccessible to other methods.

Mössbauer spectra (MS) obtained at room temperature (300 K) of MNPs  $Zn_xFe_{3-x}O_4$  ( $0 \leq x \leq 1$ ) are presented in Fig. 4, a. Figure 5, a shows the MS of MNPs  $Zn_xFe_{3-x}O_4$ , placed in an external magnetic field with a strength of 1.7 kOe, oriented parallel to a beam of gamma-radiation. Figure 6, a shows MS of MNPs  $Zn_xFe_{3-x}O_4$ , whose surface is functionalized (coated) with citric acid. Obtained from the experimental MS (Figs. 4, a, 5, a and 6, a) probability functions of the distribution of effective magnetic fields  $P(H_{\text{eff}})$  are presented in Figs. 4, b, 5, b and 6, b, respectively.

An important feature of magnetic particles is superparamagnetic relaxation, which occurs when particle sizes are so small that thermal energy overcomes the energy of anisotropy and the orientation of the magnetization of the particle changes from one direction of the light axis to another [55,56]. This feature significantly complicates the MS of MNPs  $Zn_xFe_{3-x}O_4$ , as can be seen in Figs. 4, a, 5, a and 6, a. Therefore, to process the experimental MS of MNPs  $Zn_xFe_{3-x}O_4$ , a complex procedure was used to fit and restore functions from the MS  $P(H_{\text{eff}})$  [51]. The process of such fitting includes: (1) a set of sextuplets whose relaxation times exceed the limit of the time window of the experiment ( $10^{-8}$  s), and therefore reveal blocked particles, (2) quadrupole doublets formed from superparamagnetic particles whose relaxation times are less than the value of the time window ( $10^{-8}$  s), and (3) Zeeman sextuplets with wide lines whose relaxation times are intermediate. Analysis of  $P(H_{\text{eff}})$  curves makes it possible to establish the components of sextuplets (and doublets) and draw conclusions about the belonging of these components to the corresponding iron oxides and positions of Fe ions in the crystal lattice [25,26,33,34,50]. The method of processing

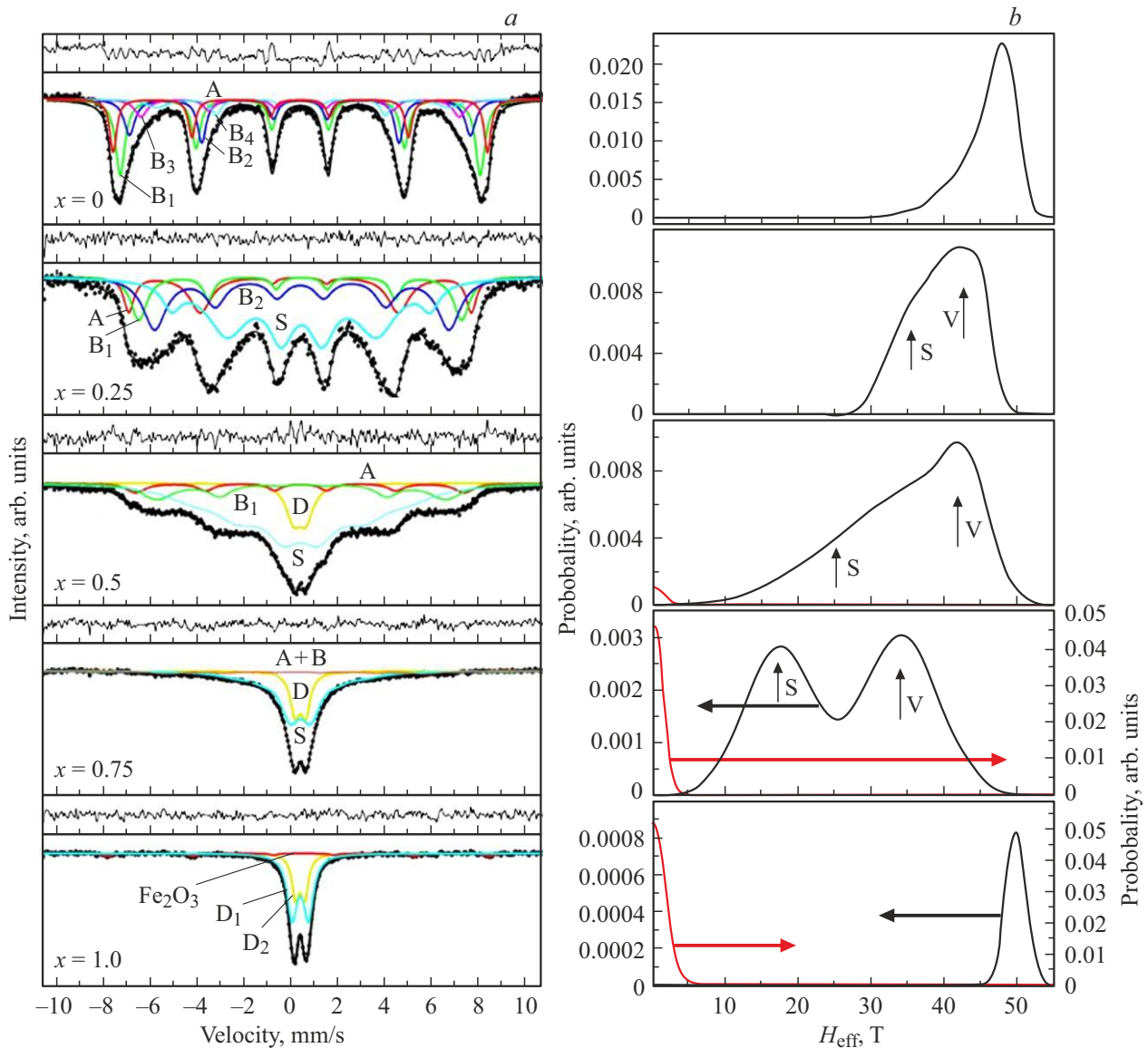


**Figure 4.** *a*) Experimental Mössbauer spectra of MNPs  $Zn_xFe_{3-x}O_4$  (for  $x = 0, 0.25, 0.5, 0.75,$  and  $1.0$ ) at room temperature and their model representations. Sextuplets, designated as A, refer to the ions Fe in the A-sublattice,  $B_i$  (where the  $i$  varies from 1 to 4) — to the Fe ions in the B-sublattice, D — Fe particle ions in the paramagnetic phase. S — Zeeman sextuplets of Fe ions in the surface layer of particles. *b*) Functions  $P(H_{\text{eff}})$  reconstructed from experimental Mössbauer spectra of MNPs  $Zn_xFe_{3-x}O_4$  using the program [51].

experimental Mössbauer spectra using the program [51] allows for their qualitative analysis [25,26,33,34,50].

The accuracy of fitting model spectra to experimental data is determined by the magnitude of the deviation of experimental values from models  $\chi^2$ , which in our cases is in the range from 1.1 to 1.2. This indicates a good coincidence of the models used with the experimental data and, consequently, the reliability of such processing of experimental spectra. Model spectra obtained by mathematical processing of experimental spectra using the program [51] are shown in continuous lines. Using the positions on the velocity scale of absorption lines, the parameters of ultrafine interactions (UFIs) were calculated, namely, isomeric shifts (IS), quadrupole

splitting (QS), effective magnetic fields  $H_{\text{eff}}$ , given in Tables 2, 3 and 4.

The values of isomeric shifts IS are given relative to the metal foil of  $\alpha$ -Fe. These tables also show the subspectrum areas (Sq) indicating the number of Fe ions at their respective positions.

#### 4.1. Mössbauer studies of MNPs $Zn_xFe_{3-x}O_4$

Mössbauer spectra (MS), obtained at room temperature (300 K) of MNPs  $Zn_xFe_{3-x}O_4$  ( $0 \leq x \leq 1$ ) without citric acid coating and in the absence of an external magnetic field, are presented in Fig. 4, *a*. It should be noted that the experimental MS of  $Zn_xFe_{3-x}O_4$  (Fig. 4, *a*) are

**Table 2.** The widths of the first and sixth lines (G) of Zeeman splitting, as well as the isomeric shifts (IS), quadrupole splitting (QS), effective magnetic fields ( $H_{\text{eff}}$ ) and subspectrum area (Sq) for iron ions at room temperature at  $\text{Zn}_x\text{Fe}_{3-x}\text{O}_4$  without coating depending on Zn ion content ( $x$ )

$\text{Zn}_x\text{Fe}_{3-x}\text{O}_4$	Component	G, mm/s	IS, mm/s	QS, mm/s	$H_{\text{eff}}$ , T	Sq, %
$x = 0$	A	$0.462 \pm 0.011$	$0.337 \pm 0.002$	$0.003 \pm 0.004$	$48.94 \pm 0.02$	31
	B <sub>1</sub>	$0.547 \pm 0.015$	$0.336 \pm 0.002$	$0.003 \pm 0.004$	$46.58 \pm 0.03$	35
	B <sub>2</sub>	$0.481 \pm 0.000$	$0.352 \pm 0.005$	$0.016 \pm 0.010$	$43.63 \pm 0.06$	15
	B <sub>3</sub>	$0.548 \pm 0.000$	$0.293 \pm 0.011$	$0.162 \pm 0.021$	$40.72 \pm 0.11$	9
	B <sub>4</sub>	$1.115 \pm 0.000$	$0.545 \pm 0.026$	$0.078 \pm 0.047$	$37.91 \pm 0.23$	11
$x = 0.25$	A	$0.527 \pm 0.129$	$0.313 \pm 0.019$	$0.032 \pm 0.036$	$45.19 \pm 0.20$	14
	B <sub>1</sub>	$0.817 \pm 0.310$	$0.371 \pm 0.020$	$0.067 \pm 0.043$	$42.55 \pm 0.33$	13
	B <sub>2</sub>	$0.940 \pm 0.390$	$0.368 \pm 0.029$	$0.062 \pm 0.051$	$38.81 \pm 0.48$	25
	S	$1.167 \pm 0.285$	$0.383 \pm 0.024$	$0.040 \pm 0.047$	$34.14 \pm 0.53$	48
$x = 0.5$	A	$1.013 \pm 0.000$	$0.305 \pm 0.027$	$0.077 \pm 0.054$	$43.09 \pm 0.16$	7
	B <sub>1</sub>	$1.801 \pm 0.184$	$0.462 \pm 0.026$	$0.192 \pm 0.054$	$37.18 \pm 0.24$	16
	S	$2.519 \pm 0.227$	$0.363 \pm 0.014$	$0.074 \pm 0.033$	$25.63 \pm 0.45$	72
	D	$0.432 \pm 0.036$	$0.343 \pm 0.006$	$0.423 \pm 0.013$	–	5
$x = 0.75$	A + B	$1.708 \pm 0.000$	$0.242 \pm 0.071$	$0.185 \pm 0.133$	$34.00 \pm 0.54$	10
	S	$1.600 \pm 0.000$	$0.354 \pm 0.039$	$0.005 \pm 0.074$	$17.30 \pm 0.60$	67
	D	$0.479 \pm 0.025$	$0.344 \pm 0.004$	$0.450 \pm 0.010$	–	24
$x = 1.0$	$\text{Fe}_2\text{O}_3$	$0.489 \pm 0.000$	$0.376 \pm 0.028$	$0.230 \pm 0.055$	$50.41 \pm 0.23$	7
	D <sub>1</sub>	$0.364 \pm 0.042$	$0.336 \pm 0.003$	$0.392 \pm 0.034$	–	31
	D <sub>2</sub>	$0.506 \pm 0.010$	$0.344 \pm 0.002$	$0.700 \pm 0.041$	–	63

similar to those obtained, for example, in [14,42,57–61]. Figure 5, *a* shows the MS of MNPs  $\text{Zn}_x\text{Fe}_{3-x}\text{O}_4$ , obtained by superimposing an external magnetic field with a strength of 1.7 kOe at room temperature. MS of MNPs  $\text{Zn}_x\text{Fe}_{3-x}\text{O}_4$ , coated with CA — MS of MNPs ( $\text{Zn}_x\text{Fe}_{3-x}\text{O}_4\text{@CA}$ ) are shown in Fig. 6, *a*. The dots on the MS (Figs. 4, *a*, 5, *a* and 6, *a*) indicate experimental values.

The MS of MNPs  $\text{Zn}_x\text{Fe}_{3-x}\text{O}_4$  are systematically changed with an increase in the amount of zinc as shown in Fig 4, *b*. So, at  $x = 0$  MS consist of wide lines of Zeeman sextuplets. An increase in the amount of Zn ( $x = 0.25$ ) leads to a decrease in intensity, a decrease in the amount of splitting and an increase in the widths of the Zeeman lines. The large widths of the Zeeman lines of the MS of  $\text{Zn}_x\text{Fe}_{3-x}\text{O}_4$  samples indicate the distribution of effective magnetic fields acting on the nuclei of  $\text{Fe}^{3+}$ , which, in turn, indicates the particle size distribution. With a further increase in the amount of zinc ( $x = 0.5$ ), there is a gradual collapse of Zeeman sextuplets and the appearance of doublet lines in the zero velocity region. At the  $x = 0.75$  on the MS of MNPs  $\text{Zn}_x\text{Fe}_{3-x}\text{O}_4$  the intensity of the lines of Zeeman sextuplets decreased

significantly (Fig. 4, *a*), and the intensity of the doublet line increased significantly, whereas at  $x = 1.0$  the Zeeman lines disappear and only the lines of the doublets are observed.

Obtained from the experimental MS of MNPs  $\text{Zn}_x\text{Fe}_{3-x}\text{O}_4$  (Fig. 4, *a*) functions  $P(H_{\text{eff}})$  (Fig. 4, *b*) differ from the functions for macrocrystals of spinel ferrites (SF) (not shown here), which observe only two maxima belonging to iron ions in two non-equivalent sublattices. On the function  $P(H_{\text{eff}})$  of MNPs  $\text{Zn}_x\text{Fe}_{3-x}\text{O}_4$  at  $x = 0$  (Fig. 4, *b*) two maxima can be distinguished, one of which (denoted as V) is at  $H_{\text{eff}} \approx 49$  T, and the other at  $H_{\text{eff}} \approx 40$  T (denoted as S). Starting from the maximum (V) at  $H_{\text{eff}} \approx 49$  T, the values of  $P(H_{\text{eff}})$  are lowered as „tail“ in the direction of reducing the effective fields. An increase in the concentration of Zn ions ( $x = 0.25$  and 0.5) leads to an elongation of this „tail“ up to  $H_{\text{eff}} \approx 10$  T at  $x = 0.5$ . This means that as the number of Zn ions increases in  $\text{Zn}_x\text{Fe}_{3-x}\text{O}_4$ , the number of small particles increases and the particle size distribution area increases. At the same time, the reduction in the size of the MNPs occurs smoothly.

**Table 3.** The widths of the first and sixth lines (G) of Zeeman splitting, as well as the isomeric shifts (IS), quadrupole splitting (QS), effective magnetic fields ( $H_{\text{exteff}}$ ) and subspectrum area (Sq) for iron ions at room temperature of MNPs  $\text{Zn}_x\text{Fe}_{3-x}\text{O}_4$  in external magnetic field with a strength of 1.7 kOe depending on Zn ion content ( $x$ )

$\text{Zn}_x\text{Fe}_{3-x}\text{O}_4$	Component	G, mm/s	IS, mm/s	QS, mm/s	$H_{\text{eff}}$ , T	Sq, %
$x = 0.0$	A	$0.427 \pm 0.025$	$0.300 \pm 0.005$	$0.051 \pm 0.010$	$48.73 \pm 0.05$	28
	B <sub>1</sub>	$0.605 \pm 0.057$	$0.330 \pm 0.006$	$0.043 \pm 0.011$	$46.50 \pm 0.08$	42
	B <sub>2</sub>	$1.123 \pm 0.102$	$0.386 \pm 0.012$	$0.108 \pm 0.025$	$41.40 \pm 0.27$	30
$x = 0.25$	A	$0.585 \pm 0.044$	$0.315 \pm 0.008$	$0.013 \pm 0.015$	$46.00 \pm 0.12$	21
	B <sub>1</sub>	$0.617 \pm 0.124$	$0.315 \pm 0.021$	$0.029 \pm 0.040$	$43.42 \pm 0.14$	13
	B <sub>2</sub>	$0.729 \pm 0.173$	$0.431 \pm 0.023$	$0.085 \pm 0.046$	$40.66 \pm 0.20$	10
	S	$1.417 \pm 0.138$	$0.362 \pm 0.010$	$0.017 \pm 0.017$	$33.62 \pm 0.42$	56
$x = 0.5$	A	$0.816 \pm 0.133$	$0.407 \pm 0.017$	$0.319 \pm 0.034$	$43.61 \pm 0.17$	15
	B <sub>1</sub>	$1.711 \pm 0.148$	$0.261 \pm 0.015$	$0.300 \pm 0.029$	$38.10 \pm 0.23$	34
	S	$4.849 \pm 0.636$	$0.287 \pm 0.032$	$0.278 \pm 0.062$	$25.84 \pm 0.38$	52
$x = 0.75$	A + B	$0.695 \pm 0.353$	$0.413 \pm 0.071$	$0.098 \pm 0.139$	$36.22 \pm 0.41$	7
	S	$2.170 \pm 0.610$	$0.338 \pm 0.036$	$0.016 \pm 0.071$	$29.49 \pm 1.03$	77
	D	$0.590 \pm 0.074$	$0.337 \pm 0.011$	$0.540 \pm 0.035$	–	16
$x = 1.0$	A + B	$0.722 \pm 0.148$	$0.521 \pm 0.039$	$0.244 \pm 0.075$	$28.09 \pm 0.27$	12
	D <sub>1</sub>	$1.555 \pm 0.208$	$0.267 \pm 0.050$	$0.689 \pm 0.229$	–	63
	D <sub>2</sub>	$0.528 \pm 0.124$	$0.353 \pm 0.014$	$0.562 \pm 0.030$	–	25

At  $x = 0.5$  in the region from 0 to 5 T on the curve  $P(H_{\text{eff}})$  a line appears, the intensity of which increases to a maximum with an increase in the content of Zn ions to  $x = 1.0$ . This line, corresponding to the doublet on the MS, indicates that at  $x = 0.5$  in the MNPs  $\text{Zn}_x\text{Fe}_{3-x}\text{O}_4$ , small particles are formed in the paramagnetic state, the magnetic blocking temperature  $T_b$  of which is higher than the room state, and the number of such particles increases when replaced with Zn ions from  $x = 0.5$  to  $x = 1.0$ . It should be noted that a doublet with similar UFI parameters was observed for  $\text{Mn}_x\text{Fe}_{3-x}\text{O}_4$  in [14].

The peak on the function  $P(H_{\text{eff}})$ , denoted as S, with an increase in the number of ions from  $x = 0$  to  $x = 0.5$  becomes better solvable and moves away from the V line towards smaller values  $H_{\text{eff}}$ . At  $x = 0.75$  on the  $P(H_{\text{eff}})$  function, two clearly resolved peaks are observed. It can be assumed that the peak, designated as V, belongs to iron ions located inside (in volume) of  $\text{Zn}_x\text{Fe}_{3-x}\text{O}_4$  particles, whereas peak S is formed by Fe ions located in the surface layer of the MNPs. The affiliation of the peak S to the Fe ions located in the surface layer of the studied particles is based on the fact that the decrease in  $H_{\text{eff}}$  of surface ions is significantly less than the change in  $H_{\text{eff}}$  when replacing the Fe ion in the crystal structure with the Zn ion. Thus, at Zn concentrations between 0.25 and 0.75 MNPs  $\text{Zn}_x\text{Fe}_{3-x}\text{O}_4$  are core/shell particles in which the

magnetically ordered core is surrounded by a shell where the superexchange interaction and therefore the effective magnetic fields are less than in the volume of the particle, as shown in [25,62,63]. Another possible explanation is the formation in the surface layer of particles of a beveled structure of magnetic moments relative to the orientation of moments in the volume of MNPs [64–66].

At  $x = 1.0$  on the function  $P(H_{\text{eff}})$  two lines are observed, the line in the region of 0–5 T indicates the presence in the sample of small particles in the paramagnetic phase. The maximum in the region  $H_{\text{eff}} \approx 50$  T refers to the Zeeman sextuplet (ZS), the analysis of the UFI parameters of which indicate its belonging to hematite (or maghemite).

Features of the functions of  $P(H_{\text{eff}})$  (Fig. 4, b) reflect the complex magnetic structure of the studied MNPs  $\text{Zn}_x\text{Fe}_{3-x}\text{O}_4$ , which cannot be explained only by the fact that when Zn ions are introduced, the distribution of ions surrounding iron ions changes.

Analysis of MS (Fig. 4, a) and functions  $P(H_{\text{eff}})$  showed that for a satisfactory description of MS of  $\text{Zn}_x\text{Fe}_{3-x}\text{O}_4$  ( $0 \leq x \leq 1.0$ ) according to the criterion  $\chi^2$ , it is necessary to use the superposition of several partial ZS and doublet. Therefore, to obtain quantitative information about the values of the parameters of ultrafine interactions, the experimental MS of MNPs  $\text{Zn}_x\text{Fe}_{3-x}\text{O}_4$  (Fig. 4, a) were processed using models individual for each concentration

**Table 4.** The widths of the first and sixth lines (G1) of the Zeeman sextuplets, as well as the isomeric shifts (IS), quadrupole splitting (QS), effective magnetic fields ( $H_{\text{exteff}}$ ) and subspectrum area (Sq) for iron ions at room temperature of MNPs functionalized with citric acid  $\text{Zn}_x\text{Fe}_{3-x}\text{O}_4\text{@CA}$ , depending on Zn ion content ( $x$ )

$\text{Zn}_x\text{Fe}_{3-x}\text{O}_4$	Component	G1, mm/s	IS, mm/s	QS, mm/s	$H_{\text{eff}}$ , T	Sq, %
$x = 0.0$	A	$0.337 \pm 0.003$	$0.330 \pm 0.001$	$-0.017 \pm 0.001$	$50.33 \pm 0.01$	17
	B <sub>1</sub>	$0.415 \pm 0.002$	$0.309 \pm 0.000$	$0.017 \pm 0.001$	$48.86 \pm 0.01$	47
	B <sub>2</sub>	$0.985 \pm 0.006$	$0.587 \pm 0.001$	$0.016 \pm 0.002$	$45.66 \pm 0.01$	36
$x = 0.25$	A	$0.382 \pm 0.013$	$0.287 \pm 0.002$	$-0.040 \pm 0.004$	$48.40 \pm 0.03$	12
	B <sub>1</sub>	$0.497 \pm 0.026$	$0.344 \pm 0.002$	$0.025 \pm 0.004$	$46.79 \pm 0.04$	27
	B <sub>2</sub>	$0.668 \pm 0.035$	$0.418 \pm 0.003$	$0.035 \pm 0.006$	$44.41 \pm 0.04$	11
	B <sub>3</sub>	$1.405 \pm 0.035$	$0.464 \pm 0.004$	$-0.024 \pm 0.007$	$41.03 \pm 0.09$	50
$x = 0.5$	A	$0.554 \pm 0.018$	$0.311 \pm 0.003$	$0.012 \pm 0.005$	$46.06 \pm 0.03$	15
	B <sub>1</sub>	$1.085 \pm 0.033$	$0.457 \pm 0.003$	$0.011 \pm 0.005$	$42.11 \pm 0.04$	55
	S	$1.308 \pm 0.062$	$0.488 \pm 0.007$	$0.057 \pm 0.013$	$36.43 \pm 0.10$	20
	D	$0.339 \pm 0.005$	$0.357 \pm 0.001$	$0.369 \pm 0.002$	–	11
$x = 0.75$	A	$0.257 \pm 0.003$	$0.371 \pm 0.001$	$0.215 \pm 0.002$	$51.55 \pm 0.01$	13
	B <sub>1</sub>	$1.727 \pm 0.075$	$0.443 \pm 0.006$	$-0.000 \pm 0.012$	$40.21 \pm 0.06$	19
	S	$6.269 \pm 0.417$	$0.475 \pm 0.013$	$-0.074 \pm 0.024$	$27.63 \pm 0.29$	50
	D	$0.309 \pm 0.002$	$0.357 \pm 0.001$	$0.369 \pm 0.001$	–	18
$x = 1.0$	D <sub>1</sub>	$0.364 \pm 0.042$	$0.336 \pm 0.003$	$0.392 \pm 0.034$	–	31
	D <sub>2</sub>	$0.506 \pm 0.010$	$0.344 \pm 0.002$	$0.700 \pm 0.041$	–	63

of Zn, differing in the number of partial sextuplets and doublets. The obtained UFI parameters are given in Table 2.

The change in ultrafine fields as a function of Zn concentration can be explained on the basis of Neel theory of molecular and superexchange fields. According to this theory, the contribution to the ultrafine magnetic field is due to the strongest exchange interactions of A–B, and the contributions due to the exchange interactions A–A or B–B are very small, and therefore they can be neglected. Ions Zn, being diamagnetic, do not participate directly in exchange interactions. The replacement of  $\text{Fe}^{3+}$  ions with  $\text{Zn}^{2+}$  weakens the superexchange interactions of  $\text{Fe}^{3+}\text{A}-\text{O}^{2-}-\text{Fe}^{3+}\text{B}$ , and therefore the ultrafine magnetic field is expected to decrease with increasing concentration of Zn ions.

The MS also shows that as particle size decreases, ultrafine magnetic fields decrease and SC line widths increase. Fluctuation of magnetization vectors in the direction close to the direction of easy magnetization leads to the dependence of ultrafine fields on particle size [55,56].

MS allows to reliably identify spectral lines belonging to the ions  $\text{Fe}^{2+}$  and  $\text{Fe}^{3+}$ , by their chemical shifts, which are  $\sim 0.2-0.5$  mm/s for  $\text{Fe}^{3+}$  and  $\sim 0.9-1.1$  mm/s for  $\text{Fe}^{2+}$  [67]. However, in the case of SF MNPs, the IS

values belonging to iron ions in the high-spin state of  $\text{Fe}^{3+}$ , as a rule, are in the range of 0.3–0.6 mm/s [50]. There are not higher values of the chemical shifts (from 0.9 to 1.1 mm/s), which belong to the Fe ions in the low-spin state of  $\text{Fe}^{2+}$ . As can be seen from Table 2, IS values are in the range of 0.3–0.5 mm/s. This means that in the studied MNPs  $\text{Zn}_x\text{Fe}_{3-x}\text{O}_4$  there are only iron ions in the high-spin state of  $\text{Fe}^{3+}$ . According to Table 2, the IS values for various ZS differ little, and this does not allow to identify the belonging of lines to non-equivalent positions of Fe ions on the basis of IS. Therefore, the identification of the ZS is based on the results of the works [68,69] which showed that in the SF  $M\text{Fe}_2\text{O}_4$  ( $M$  — metal ions) the ultrafine magnetic field of Fe ions in A-nodes is greater than in B-nodes. Therefore, in the MNPs  $\text{Zn}_x\text{Fe}_{3-x}\text{O}_4$  (Fig. 4, a) ZS with a maximum value of  $H_{\text{eff}}$  represents the ions  $\text{Fe}^{3+}$  at position A. The remaining ZS ( $\text{B}_i$ , where  $i$  varies from 1 to 4) with smaller  $H_{\text{eff}}$  characterize  $\text{Fe}^{3+}$  ions at position B having different environments.

The average  $T_b$  in Mössbauer experiments is defined as the temperature at which half of all iron atoms have a magnetic moment fixed in space during the measurement timeline, which on the MS is observed as Zeeman

components (blocked behavior), whereas for the other half the moments oscillate, giving a pure zero value and observed on the MS as a doublet line (unblocked behavior) [70]. On the spectra of  $Zn_xFe_{3-x}O_4$  at  $0 \leq x \leq 0.25$ , only the ZS lines are observed, and at  $0.25 < x \leq 0.75$  there are lines of doublets whose area is significantly less than the area of the ZS, indicating that the blocking temperature of these particles is above 300 K. In the case of the MNPs  $ZnFe_2O_4$  ( $x = 1.0$ ), the ZS area is much smaller than the area of the doublets, indicating that  $T_b$  is significantly lower than room temperature. At temperatures below  $T_b$ , each value of the ultrafine field can be related to the volume of the particle [64], so the field distribution  $P(H_{\text{eff}})$  can be converted to the particle size distribution.

#### 4.2. Mössbauer studies of MNPs $Zn_xFe_{3-x}O_4$ in external magnetic field

Mössbauer studies of samples in strong (tens of tesla strength) external magnetic fields (EMFs) obtained new unique information about the existence of non-collinearity of magnetic moments on the surface of the MNPs relative to the moments of Fe ions located in the volume of the particle [70,71]. In addition, the use of strong EMFs can significantly increase the resolution of the ZS lines and, consequently, the accuracy of MS processing and the distribution of Fe ions at non-equivalent positions of the crystal lattice [70–72].

A significant influence of weak magnetic fields (on the order of or less than 1 kOe) on the shape of the Mössbauer spectra of MNPs was observed as early as the late 1960s [73,74]. In theoretical insights, it was shown that the Mössbauer spectroscopy with the superimposition of weak EMFs (with a strength of hundreds Oe) allows us to study the dynamic effects associated with the processes of fluctuation of the magnetic moment and transition to the paramagnetic state, since in the EMFs the ultrafine structure of the superparamagnet stabilizes and increases the spin relaxation time (see, for example, [75,76]).

In this regard, the Mössbauer measurements of the MNPs  $Zn_xFe_{3-x}O_4$  at room temperature were carried out when the EMFs was applied with a strength of 1.7 kOe, parallel to the gamma-radiation beam. The experimental MS of MNPs  $Zn_xFe_{3-x}O_4$  (Fig. 4, a) changed significantly when applying the EMFs (Fig. 5, a). The large MS line widths of  $Zn_xFe_{3-x}O_4$  samples in the EMFs also indicate the distribution of  $H_{\text{eff}}$  acting on the cores of  $Fe^{3+}$  in the nanoparticles, which, in turn, indicates the particle size distribution in the samples under study. Using the procedure [51], the MS (Fig. 5, a) were decomposed into partial sextuplets and doublets corresponding to the distribution of the ultrafine field ( $H_{\text{hf}}$ ), shown in Fig. 5, a in solid lines. The  $P(H_{\text{eff}})$  functions obtained from the MS (Fig. 5, a) and the UFI parameters are shown in Fig. 5, b and in Table 3, respectively.

On the MS of MNPs  $Zn_xFe_{3-x}O_4$ , measured in EMFs at  $x = 0$  (Fig. 5, a), the best resolution of spectral lines is observed compared to MS of MNPs  $Zn_xFe_{3-x}O_4$  (Fig. 4, a), because the intensities of the second and fifth lines of the ZS have significantly decreased due to the parallelism of the EMFs to beam of gamma-radiation. An increase in the amount of Zn ( $x = 0.25$ ) leads to a decrease in the intensity and increase in the widths of the Zeeman lines, as well as a decrease in the amount of ZS splitting.

A further increase in the amount of zinc ( $x = 0.5$ ) leads to a gradual „collapse“ of ZS and the appearance of doublet lines in the zero velocity region. At  $x = 0.75$  and 1.0, the intensities of the doublet lines increased significantly, while the intensities of the ZS lines decreased, but unlike the MS of  $Zn_xFe_{3-x}O_4$  without EMFs, they did not disappear completely. This indicates the stabilization of relaxation processes in the studied particles  $Zn_xFe_{3-x}O_4$  when applying EMFs. Unfortunately, the EMFs intensity of 1.7 kOe is insufficient for better resolution of spectral lines and calculation of the distribution of iron ions from MS to non-equivalent positions of the crystal lattice.

The  $P(H_{\text{eff}})$  functions, derived from the MS of MNPs  $Zn_xFe_{3-x}O_4$  in the EMFs (Fig. 5, a) are shown in Fig. 5, b, and they differ from the functions restored for MNPs  $Zn_xFe_{3-x}O_4$  without the EMFs (Fig. 4, b). So, when  $x = 0$  (Fig. 5, b), on the function  $P(H_{\text{eff}})$ , you can select two peaks, denoted V and S. The formation of these peaks is due to the reasons discussed in detail in paragraph 4.2. Small differences are explained by the fact that the external magnetic field stabilizes the dynamics of the behavior of particles in the superparamagnetic region. Thus, when measuring without EMFs, the two-humped curve ( $x = 0.75$ ) is observed in the range from 5 to 47 T, whereas when measuring in EMFs such a curve is observed in the region  $H_{\text{eff}}$  from 16 to 42 T (Fig. 5, b). In addition, the line in the region from 0 to 5 T appears at  $x = 0.5$  (measurements without EMFs, Fig. 4, b), and when measured in EMFs, this line is observed at  $x = 0.75$  (Fig. 5, b), and its intensity increases with an increase in the proportion of Zn ions to 1.0. All this indicates that the EMFs stabilize the dynamics of the superparamagnetic behavior of the MNPs  $Zn_xFe_{3-x}O_4$ . The line belonging to magnetite (or maghemite) observed for the MNPs  $ZnFe_2O_4$  (Fig. 4, b) is absent on the MS of MNPs  $ZnFe_2O_4$ , obtained by applying the EMFs. This is probably due to the fact that the intensity of the magnetite (or maghemite) lines is so small that they are not observed on the MS in the EMFs against the background of the field-induced ZS.

Thus, Mössbauer studies in the EMFs also indicate that at Zn concentrations of 0.25 to 0.5 MNPs  $Zn_xFe_{3-x}O_4$  are particles consisting of a magnetically ordered nucleus and shell in which the superexchange interaction and, therefore, the effective magnetic fields are less than in the volume of the particle, or in the surface layer a beveled structure of magnetic moments relative to moments in the volume of MNPs is formed.

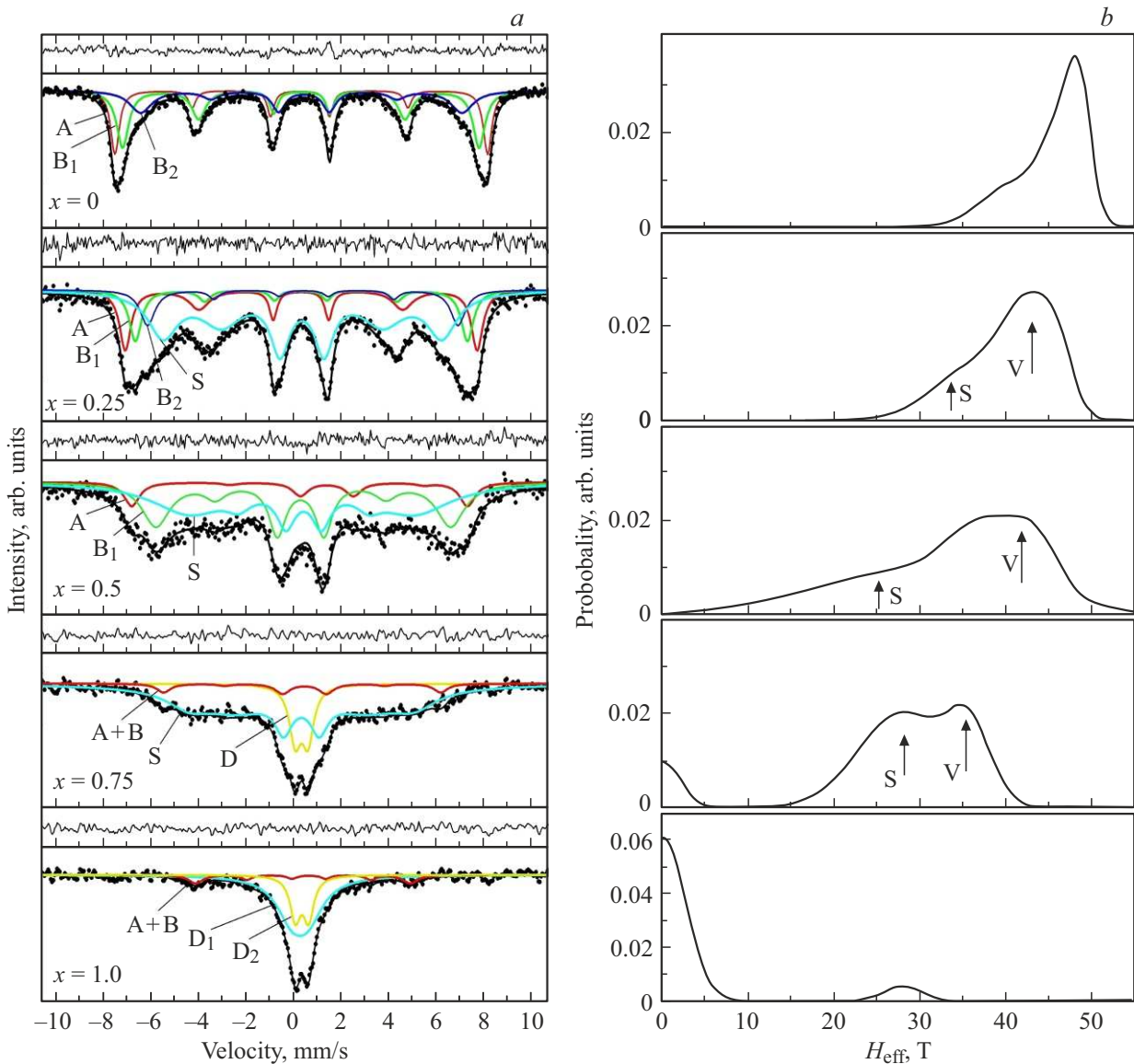


**Figure 5.** a) Experimental Mössbauer spectra of MNPs  $\text{Zn}_x\text{Fe}_{3-x}\text{O}_4$  (for  $x = 0, 0.25, 0.5, 0.75$  and  $1.0$ ) at room temperature in an external magnetic field with a strength of  $1.7\text{ kOe}$  and their model representation. Sextuplets, designated as A, refer to the ions Fe in the A-sublattice,  $B_i$  (where the  $i$  varies from 1 to 4) — to the Fe ions in the B-sublattice, D — Fe particle ions in the paramagnetic phase. A+B — the ZS of Fe ions in the surface layer of the particles. b) Functions  $P(H_{\text{eff}})$  reconstructed from experimental Mössbauer spectra of MNPs  $\text{Zn}_x\text{Fe}_{3-x}\text{O}_4$ , using the program [51].

#### 4.3. Mössbauer studies of MNPs $\text{Zn}_x\text{Fe}_{3-x}\text{O}_4$ coated with citric acid $\text{Zn}_x\text{Fe}_{3-x}\text{O}_4\text{@CA}$

In order to study the effect of surface functionalization by citric acid on the properties of  $\text{Zn}_x\text{Fe}_{3-x}\text{O}_4$  particles, MS of MNPs  $\text{Zn}_x\text{Fe}_{3-x}\text{O}_4\text{@CA}$  ( $0 \leq x \leq 1$ ) were removed at  $300\text{ K}$ , shown in Fig. 6, a. The probabilities of the distribution  $H_{\text{eff}}$  and the calculated parameters of the UFIs are presented in Fig. 6, b and in Table 4, respectively, restored from the experimental MS.

MS of MNPs coated with citric acid  $\text{Zn}_x\text{Fe}_{3-x}\text{O}_4\text{@CA}$  (Fig. 6, a), differ significantly from the MS of uncovered MNPs  $\text{Zn}_x\text{Fe}_{3-x}\text{O}_4$  (Fig. 4, a). So, at  $x = 0$ , the widths

of the ZS lines are quite narrow and the resolution is good enough. This allows us to describe them with three ZSS. Substitution with Zn ions ( $x = 0.25$  and  $x = 0.5$ ) leads to a significant increase in the widths of the ZS, indicating the distribution of  $H_{\text{eff}}$ , which, in turn, indicates the particle size distribution. This also reduces the width of the splitting of the ZS, which means a decrease in particle sizes. On the MS of  $\text{Zn}_x\text{Fe}_{3-x}\text{O}_4\text{@CA}$  at  $0 \leq x \leq 0.25$ , only the ZS lines are observed, indicating that in these particles  $T_b$  below room temperature. At  $x = 0.5$  against the background of the ZS, a clearly allowed doublet is observed, the intensity of which increases with an increase in Zn, and at  $x = 1.0$  only the lines of the doublet remain.

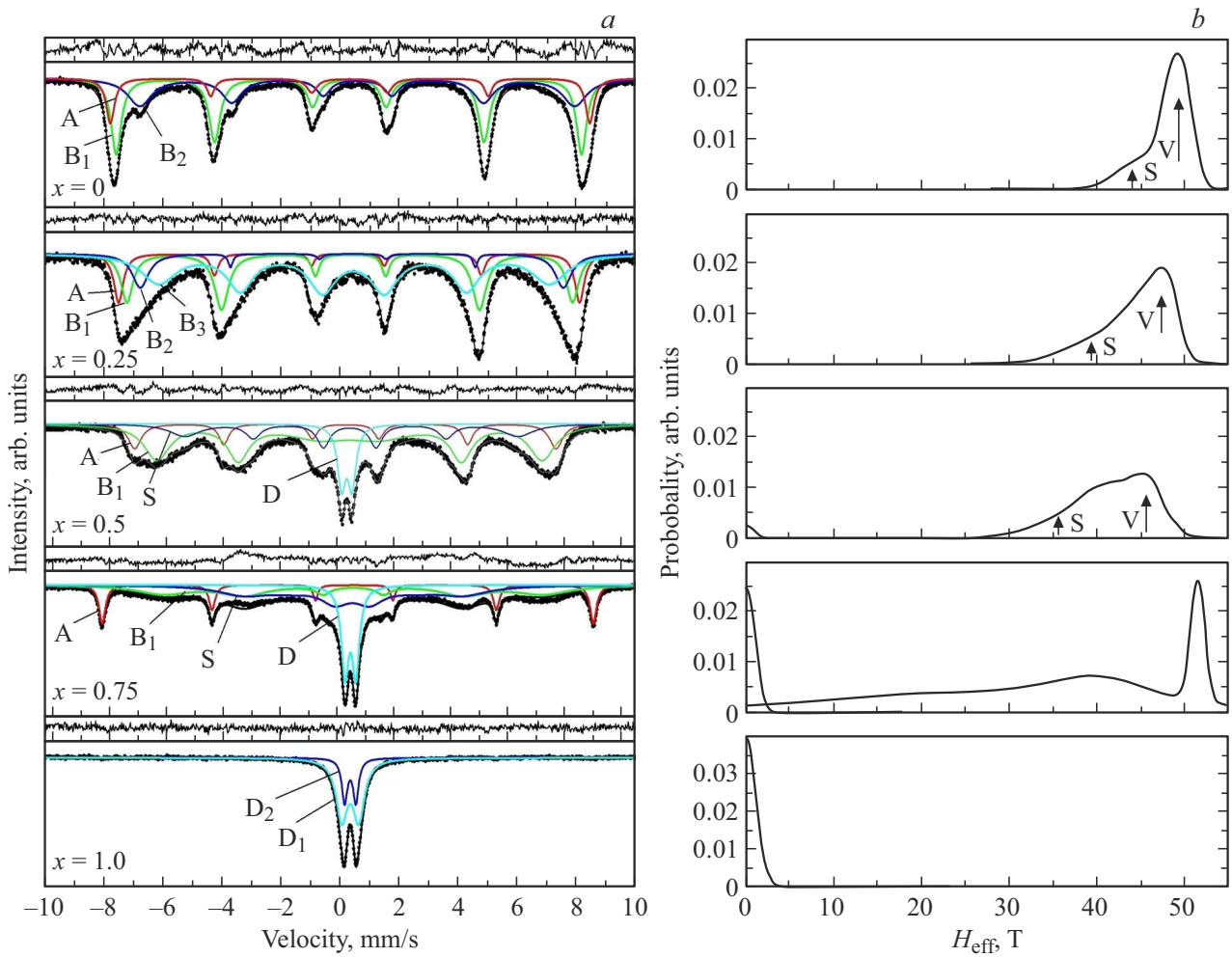


**Figure 6.** *a*) Experimental Mössbauer spectra of room temperature MNPs coated with citric acid  $Zn_xFe_{3-x}O_4@CA$  (for  $x = 0, 0.25, 0.5, 0.75$  and  $1.0$ ) and their model representations. The sextuplet for iron ions in the tetrahedral sublattice is denoted by the letter A, in the octahedral sublattices —  $B_1, B_2$  and  $B_3$ , and the doublets defined by paramagnetic phase particles — D. *b*) Functions  $P(H_{\text{eff}})$  reconstructed from the experimental Mössbauer spectra of MNPs  $Zn_xFe_{3-x}O_4@CA$  using the program [51].

MS of MNPs  $Zn_xFe_{3-x}O_4@CA$  at  $x = 0.75$  is described by three ZSS, one of which has clearly defined lines, and the UFI parameters of this sextuplet indicate its belonging to hematite (or maghemite), which is consistent with the XRD data. The intensities of the lines of the second ZS at  $x = 0.75$  (Fig. 6, *a*) are insignificant, and the value of  $H_{\text{eff}} \approx 40$  T suggests that this ZS refers to Fe ions located in the volume of MNPs  $Zn_{0.75}Fe_{2.25}O_4$ . A value of  $H_{\text{eff}}$  of the third sextuplet, equal to  $\sim 28$  T, indicates that this ZS belongs to the iron ions in the surface layer of these particles.

At  $x = 1.0$ , the ZS lines disappear completely, and the MS, as can be seen in Figs. 4, *a, 5, a* and 6, *a*, as well as in Tables 3, 4 and 5, are described in two doublets belonging to the  $Fe^{3+}$  ions. The statement that iron ions are in a high-spin state is based on the values of isomeric shifts corresponding to the ions  $Fe^{3+}$  [67]. The affiliation of doublets to A- or B-sublattices was determined by the values of isomeric shifts, namely, a doublet with a smaller isomeric shift refers

to iron ions in a tetrahedral A-position. A smaller isomeric shift for Fe ions in A-positions than in B-positions is formed from -due to the higher covalence of the Fe–O bond in A-position.

On the probability functions of the distribution of effective magnetic fields  $P(H_{\text{eff}})$ , recovered from MS of functionalized MNPs  $Zn_xFe_{3-x}O_4@CA$  (Fig. 6, *b*), at  $x < 0.5$ , one can observe a curve, „the tail“ of which, with an increase in the concentration of Zn stretches out towards smaller  $H_{\text{eff}}$ . However, this elongation of the „tail“ is less than in the case of the particles  $Zn_xFe_{3-x}O_4$ . This means that increasing the amount of Zn to  $x = 0.5$  leads to an increase in the particle distribution of  $Zn_xFe_{3-x}O_4@CA$  by size, but it is significantly smaller than for particles  $Zn_xFe_{3-x}O_4$ . At these concentrations of Zn on the functions  $P(H_{\text{eff}})$  two maxima can be distinguished, indicated in Fig. 6, *b* with arrows with the letters V and S. Peak V refers to ions Fe in the volume of MNPs. Shifting this maximum in the direction of lower values  $H_{\text{eff}}$  means a decrease in particle

size. Another peak S belongs to the Fe ions in the surface layer of the MNPs. An increase in the intensity of the peak S in the region of  $0 \leq x \leq 0.5$  means an increase in the thickness of this surface layer and a decrease in particle sizes. At  $x = 0.5$ , a line appears in the region of effective fields from 0 to 5 T, indicating that with such a number of Zn ions particles are formed in the paramagnetic phase. With an increase in the concentration of Zn substitute ions, the intensity of this line increases, which means an increase in the number of particles in the paramagnetic state.

At  $x = 0.75$ , there are three peaks on the  $P(H_{\text{eff}})$  function. The peak at 35 T belongs to iron ions located inside the particles  $\text{Zn}_{0.75}\text{Fe}_{2.25}\text{O}_4$ , while the peak in the region of 17.5 T is formed by Fe ions located in the surface layer of the MNPs. A low-intensity line in the region 52 T indicates the presence of a small number of hematite (or maghemite) particles in the magnetically ordered state, which is consistent with the data of XRD studies. For  $x = 1.0$  on the function  $P(H_{\text{eff}})$  a peak no need observed only in the region 0–5 T, indicating that MNPs  $\text{ZnFe}_2\text{O}_4$  consists of small particles in the paramagnetic state observed at MS (Fig. 6, a) with doublet lines.

The results of Mössbauer studies of functionalized MNPs  $\text{Zn}_x\text{Fe}_{3-x}\text{O}_4@CA$  also indicate that with substitution values from 0 to 0.75, these MNPs are particles of the nucleus/shell type. In this case, the nucleus is in a magnetically ordered state, while the shell is in the magneto-unordered phase, because the superexchange interaction and, consequently, the effective magnetic fields in the surface layer are less than in the volume of the particle, or in the surface layer a beveled structure of magnetic moments is formed relative to the moments in the volume of the MNPs.

With an increase in the concentration of Zn ions, the intensities of the sextuplets lines decrease, the distance between the sextuplets lines decreases, and at a concentration of  $x = 0.25$  and above, they begin to „collapse“. On MS of  $\text{Zn}_x\text{Fe}_{3-x}\text{O}_4$ , coated with CA, at a concentration of  $x = 0.5$  and above, doublets with narrow lines are observed. On MS of MNPs  $\text{Zn}_x\text{Fe}_{3-x}\text{O}_4$ , covered with CA (at  $x = 0.75$ ), Zeeman sextuplets (ZS) are observed, one of which is clearly expressed because it has narrow lines. The analysis showed that the UFI parameters of this sextuplet are similar to the parameters of hematite. Therefore, when  $\text{Zn}_{0.75}\text{Fe}_{2.25}\text{O}_4$  particles are coated with citric acid, hematite (or maghemite) is formed ( $\alpha\text{-Fe}_2\text{O}_3$ ), the proportion of which in the sample is  $\sim 13\%$ .

Analysis of MS and  $P(H_{\text{eff}})$  functions for  $\text{Zn}_x\text{Fe}_{3-x}\text{O}_4$  particles (Fig. 4) and  $\text{Zn}_x\text{Fe}_{3-x}\text{O}_4@CA$  (Fig. 6) indicate that coating of the particles with CA leads to their isolation from each other, reducing or eliminating interactions between the particles. It is important that the coating of the particles leads to a decrease in the thickness of the paramagnetic shell, and due to this, the diameter of the magnetically ordered core increases. Coating leads to a decrease in the blocking temperature, as observed in [77].

## 5. Size estimation of synthesized MNPs

Comparison of the obtained results with the published Mössbauer data on particles  $\text{Zn}_x\text{Fe}_{3-x}\text{O}_4$  allows us to estimate the size of the MNPs studied. So in the studies [14,42,57–61], the results of Mössbauer studies of MNPs  $\text{MnFe}_2\text{O}_4$  with sizes from 3 to 98 nm are presented. MS of MNPs  $\text{Zn}_x\text{Fe}_{3-x}\text{O}_4$ , whose dimensions according to the results of the XRD ranged from 21 to 7 nm [14], with Zn substitution values greater than 0.2 are similar to the MS shown in Fig. 4, a, with the same Zn content. With smaller amounts of Zn ions, the ZS of non-equivalent sublattices observed in [14] are allowed — unlike the MS shown in Fig. 4, a, on which there is no resolution, indicating that the particle sizes are less than 21 nm. Mössbauer spectroscopy data obtained during the study of  $\text{Zn}_x\text{Fe}_{3-x}\text{O}_4$  particles with sizes from 15 to 117 nm indicate that on the MS of particles of 15 nm at  $x = 0.5$  against the background of the ZS, a quadrupole doublet is observed, and with an increase in particle size, the intensity of the ZS lines increases [42]. In the same study [42] on particles  $\text{Fe}_3\text{O}_4$  ( $x = 0$ ) with dimensions of 38 nm MS was obtained with split lines of ZS non-equivalent sublattices and the absence of a paramagnetic doublet. In [57] on particles  $\text{Zn}_x\text{Fe}_{3-x}\text{O}_4$ , the size of which increases from 40 nm (at  $x = 0.0$ ) to 42 nm (at  $x = 1.0$ ), doublet for the sample  $x = 1.0$  even at the temperature of liquid nitrogen was observed on MS. This means that  $T_b$  is below 77 K. Mössbauer particle measurements of  $\text{Zn}_x\text{Fe}_{3-x}\text{O}_4$  with dimensions  $\sim 40$  nm demonstrated MS with splitting of Zeeman lines for non-equivalent sublattices up to  $x = 0.5$ , and at  $x = 1$ , the spectrum consists of a quadrupole doublet [57]. On the MS of particles  $\text{Fe}_3\text{O}_4$  with dimensions of 5.3 nm a wide singlet is observed, whereas in the case of particles of size 11 nm there is a ZS with a fairly good resolution of lines [58]. Obtained in [59] MS of MNPs  $\text{Zn}_x\text{Fe}_{3-x}\text{O}_4$  (at  $0.01 \leq x \leq 0.8$ ) for sizes from 3 to 10 nm are similar to those shown in Fig. 4, a.

Analysis of the obtained experimental MS and comparison with the data published in the literature allows us to conclude that when doped by Zn ions from  $x = 0$  to  $x = 1.0$ , the dimensions of the MNPs  $\text{Zn}_x\text{Fe}_{3-x}\text{O}_4$  smoothly change from 15 to 5 nm, which is not consistent with the results of the XRD studies given in Fig. 2.

## 6. Conclusion

Magnetic nanoparticles  $\text{Zn}_x\text{Fe}_{3-x}\text{O}_4$  (where  $x = 0, 0.25, 0.5, 0.75, 1$ ) were synthesized by the hydrothermal method, which were then coated with citric acid (CA). Comprehensive studies of the properties of the obtained MNPs were carried out using XRD, magnetic and Mössbauer measurements, depending on both the content of Zn ions and their changes during the functionalization of CA particles. X-ray diffractograms and Mössbauer spectra showed that the synthesized MNPs are single-phase, have

no foreign impurities and are in a superparamagnetic state. The XRD data indicate an increase in the size of the MNPs from 17 to 34 nm with an increase in the concentration of Zn from  $x = 0.25$  to  $x = 0.75$ . Analysis of the obtained and published Mössbauer data showed that the size of the MNPs gradually decreases from 15 to 5 nm when replaced with Zn ions from  $x = 0$  to  $x = 1.0$ . No differences in the properties of CA-coated and uncoated MNPs were detected by the XRD method. Data from Mössbauer studies indicate that coating of the particles with CA leads to their isolation from each other, reducing or eliminating interactions between particles, reducing the thickness of the paramagnetic shell and, thereby, increasing the diameter of the nucleus.  $T_b$  of the particles is lowered when coating.

Thus, using the samples of the MNPs  $Zn_xFe_{3-x}O_4$ , a simple strategy of functionalization and modification of the surface to create new multifunctional biocompatible materials with superparamagnetism was demonstrated. Citric acid coated MNPs  $Zn_xFe_{3-x}O_4@CA$  due to the combination of functionalization, biocompatibility and superparamagnetism are promising for biomedical applications, in particular drug delivery, magnetic hyperthermia, enhancement of image contrast.

## Funding

N. Dogan and A. Bingolbali express their gratitude for the financial support of the Scientific and Technological Research Council of Turkey (TUBITAK grants: No. 115E776 and No. 115E777).

## Conflict of interest

The authors declare that they have no conflict of interest.

## References

- [1] C.M. Hussain. Handbook of Nanomaterials for Industrial Applications. Elsevier Inc., Amsterdam, Netherlands (2018). 709 p.
- [2] K. Zhu, Y. Ju, J. Xu, Z. Yang, S. Gao, Y. Hou. Acc. Chem. Res. **51**, 2, 404 (2018).
- [3] S. Dey, S.K. Dey, K. Bagani, S. Majumder, A. Roychowdhury, S. Banerjee, V.R. Reddy, D. Das, S. Kumar. Appl. Phys. Lett. **105**, 6, 063110 (2014).
- [4] B. Aslibeiki, P. Kameli, H. Salamati, G. Concas, M.S. Fernandez, A. Talone, G. Muscas, D. Peddis. Beilstein J. Nanotechnol. **10**, 856 (2019).
- [5] A. Kaur, G.K. Bhargava. Mater. Today: Proc. **37**, Part 2, 3082 (2021).
- [6] Clinical Applications of Magnetic Nanoparticles / Ed. N.T.K. Thanh. CRC Press Taylor & Francis Group (2018). 495 p.
- [7] L. Peixoto, R. Magalhães, D. Navas, S. Moraes, C. Redondo, R. Morales, J.P. Araújo, C.T. Sousa. Appl. Phys. Rev. **7**, 1, 011310 (2020).
- [8] M.M. Cruz, L.P. Ferreira, J. Ramos, S.G. Mendo, A.F. Alves, M. Godinho, M.D. Carvalho. J. All. Comp. **703**, 370 (2017).
- [9] K. Islam, M. Haque, A. Kumar, A. Hoq, F. Hyder, S.M. Hoque. Nanomater. **10**, 11, 2297 (2020).
- [10] V. Narayanaswamy, I.A. Al-Omari, A.S. Kamzin, B. Issa, H.O. Tekin, H. Khourshid, H. Kumar, A. Mallya, S. Sambasivam, I.M. Obaidat. Nanomater. **11**, 5, 1231 (2021).
- [11] M. Wen, Q. Li, Y. Li. J. Electron Spectroscop. Rel. Phenomena **153**, 3, 65 (2006). DOI: 10.1016/j.elspec.2006.06.002
- [12] P. Thakur, D. Chahar, S. Taneja, N. Bhalla, A. Thakur. Ceram. Int. **46**, 10, 15740 (2020).
- [13] I. Sharifi, H. Shokrollahi, S. Amiri. J. Magn. Magn. Mater. **324**, 6, 903 (2012).
- [14] J.M. Byrne, V.S. Coker, E. Cespedes, P.L. Wincott, D.J. Vaughan, R.A.D. Patrick, G. van der Laan, E. Arenholz, F. Tuna, M. Bencsik, J.R. Lloyd, N.D. Telling. Adv. Funct. Mater. **24**, 2518 (2014). DOI: 10.1002/adfm.201303230
- [15] V. Šepelák. Ann. Chim. Sci. Mater **27**, 6, 61 (2002).
- [16] T. Hyeon, S.S. Lee, P.J. Chung Y, H.B. Na. J. Am. Chem. Soc. **123**, 51, 12798 (2001).
- [17] Y.B. Kholam, S.R. Dhage, H.S. Potdar, S.B. Deshpande, P.P. Bakare, S.D. Kulkarni, S.K. Date. Mater. Lett. **56**, 571 (2001).
- [18] Y. Lee, J. Lee, C.-J. Bae, J.-G. Park, H.-J. Noh, J.-H. Park, T. Hyeon. Adv. Funct. Mater. **15**, 3, 503 (2005).
- [19] A.K. Gupta, M. Gupta. Biomaterials **26**, 18, 3995 (2005).
- [20] J. Bennet, R. Tholkappian, K. Vishista, N.V. Jaya, F. Hamed. Appl. Surf. Sci. **383**, 113 (2016). <https://doi.org/10.1016/j.apsusc.2016.04.177>
- [21] T. Vigneswari, P. Raji. Inorg. Nano-Metal Chem. **49**, 354 (2019). <https://doi.org/10.1080/24701556.2019.1661453>
- [22] H. Mahajan, S.K. Godara, A.K. Srivastava. J. Alloys. Compounds **896**, 162966 (2021).
- [23] E.A. Périgo, G. Hemery, O. Sandre, D. Ortega, E. Garaió, F. Plazaola, F.J. Teran. Appl. Phys. Rev. **2**, 4, 041302 (2015). DOI: 10.1063/1.4935688
- [24] E. Umut, M. Coşkun, H. Güngüneş, V. Dupuis, A.S. Kamzin. J. Supercond. Nov. Magn. **34**, 3, 913 (2021). DOI: 10.1007/s10948-020-05800-y
- [25] A.S. Kamzin, I.M. Obaidat, A.A. Valliulin, V.G. Semenov, I.A. Al-Omari. FTT **62**, 10, 1715 (2020) (in Russian). DOI: 10.21883/FTT.2020.10.49928.056
- [26] A.S. Kamzin, I.M. Obaidat, A.A. Valliulin, V.G. Semenov, I.A. Al-Omari. FTT **62**, 11, 1919 (2020) (in Russian). DOI: 10.21883/FTT.2020.11.50071.062
- [27] M.A. Dheyab, A.A. Aziz, M.S. Jameel, O. Abu Noqta, P. Moradi Khaniabadi, B. Mehrdel. Sci. Rep. **10**, 1, 10793 (2020). DOI: 10.1038/s41598-020-67869-8
- [28] E. Cheraghipour, S. Javadpour, A.R. Mehdizadeh. J. Biomed. Sci. Eng. **5**, 12, 715 (2012).
- [29] H. Gupta, P. Paul, N. Kumar, S. Baxi, D.P. Das. J. Colloid Interface Sci. **430**, 221 (2014).
- [30] C. Scharlach, C. Warmuth, E. Schellenberger. Magn. Res. Imaging **33**, 9, 1173 (2015).
- [31] P.H. Linh, N.X. Phuc, L.V. Hong, L.L. Uyen, N.V. Chien, P.H. Nam, N.T. Quy, H.T.M. Nhung, P.T. Phong, I.J. Lee. J. Magn. Magn. Mater. **460**, 128 (2018). <https://doi.org/10.1016/j.jmmm.2018.03.065>
- [32] V. Narayanaswamy, I.M. Obaidat, A.S. Kamzin, S. Latiyan, S. Jain, H. Kumar, C. Srivastava, S. Alaabed, B. Issa. Int. J. Mol. Sci. **20**, 13, 3368 (2019). DOI: 10.3390/ijms20133368

- [33] A.S. Kamzin, I.M. Obaidat, V.S. Kozlov, E.V. Voronina, V. Narayanaswamy, I.A. Al-Omari. *FTT* **63**, 6, 807 (2021) (in Russian). DOI: 10.21883/FTT.2021.06.50944.004
- [34] A.S. Kamzin, I.M. Obaidat, V.S. Kozlov, E.V. Voronina, V. Narayanaswamy, I.A. Al-Omari. *FTT* **63**, 7, 900 (2021) (in Russian). DOI: 10.21883/FTT.2021.07.51040.039
- [35] M. Amiri, M. Salavati-Niasari, A. Akbari. *Adv. Colloid Interface Sci.* **265**, 29 (2019). <https://doi.org/10.1016/j.cis.2019.01.003>
- [36] L.O. Lanier, O.I. Korotych, A.G. Monsalve, D. Wable, S. Savliwala, N.W.F. Grooms, C. Nacea, O.R. Tuijt, J. Dobson. *Int. J. Hyperthermia* **36**, 687 (2019). DOI: 10.1080/02656736.2019.1628313
- [37] G.Yu. Vasyukov, I.V. Mitrofanova, V.V. Ivanova, V.D. Prokopyeva. *Byull. Sibirskoi meditsiny* **13**, 6, 33 (2014) (in Russian).
- [38] Y. Piñero-Redondo, M. Bañobre-López, I. Pardiñas-Blanco, G. Goya, M.A. López-Quintela, J. Rivas. *Nanoscale Res. Lett.* **6**, 1, 383 (2011). DOI: 10.1186/1556-276x-6-383
- [39] C. Nayek, K. Manna, G. Bhattacharjee, P. Murugavel, I. Obaidat. *Magnetochem.* **3**, 2, 19 (2017). DOI: 10.3390/magnetochemistry3020019
- [40] M.A.A. Kerroum, C. Iacovita, W. Baaziz, D. Ihiawakrim, G. Rogez, M. Benaissa, C.M. Lucaci, O. Ersen. *Int. J. Mol. Sci.* **21**, 20, 7775 (2020). DOI: 10.3390/ijms21207775
- [41] A. Hanini, L. Lartigue, J. Gavard, K. Kacem, C. Wilhelm, F. Gazeau, F. Chau, S. Ammar. *J. Magn. Magn. Mater.* **416**, 315 (2016). <https://doi.org/10.1016/j.jmmm.2016.05.016>
- [42] P.M. Zélis, G.A. Pasquevich, S.J. Stewart, M.B.F. Van Raap, J. Apesteguy, I.J. Bruvera, C. Laborde, B. Pianciola, S. Jacobo, F.H. Sánchez. *J. Phys. D* **46**, 12, 125006 (2013). <https://doi.org/10.1088/0022-3727/46/12/125006>.
- [43] J.-T. Jang, H. Nah, J.-H. Lee, S.H. Moon, M.G. Kim, J. Cheon. *Angew. Chem. Int. Ed.* **48**, 7, 1234 (2009). <https://doi.org/10.1002/anie.200805149>
- [44] M.A. Daniele, M.L. Shaughnessy, R. Roeder, A. Childress, Y.P. Bandera, S. Foulger. *ACS Nano* **7**, 1, 203 (2012).
- [45] C. Liu, P. Huang. *Soil Sci. Soc. Am. J.* **63**, 1, 65 (1999).
- [46] T.J. Daou, G. Pourroy, S. Bégin-Colin, J.M. Grenéche, C. Ulhaq-Bouillet, P. Legar, P. Bernhardt, C. Leuvrey, G. Rogez. *Chem. Mater.* **18**, 18, 4399 (2006).
- [47] S. Xuan, L. Hao, W. Jiang, X. Gong, Y. Hu, Z. Chen. *J. Magn. Magn. Mater.* **308**, 210 (2007).
- [48] *Mössbauer Spectroscopy Applied to Magnetism and Materials Science* / Eds G.J. Long, F. Grandjean. Springer Science+Business Media, N.Y. (1996). V. 1. 479 p.
- [49] V. Kuncser, O. Crisan, G. Schinteie, F. Tolea, P. Palade, M. Valeanu, G. Filoti. *Modern Trends in Nanoscience*. Editura Academiei Romane. Bucharest. V. 197. (2013).
- [50] A.S. Kamzin, I.M. Obaidat, V.G. Semenov, V. Narayanaswamy, I.A. Al-Omari, B. Issa, I.V. Buryanenko. *FTT* **64**, 6, 712 (2022) (in Russian).
- [51] V.G. Semenov, V.V. Panchuk. The Mössbauer Spectra Processing MossFit software. Private message.
- [52] M. Abbas, B. Parvatheeswara Rao, S.M. Naga, M. Takahashi, C. Kim. *Ceram. Int.* **39**, 7, 7605 (2013). DOI: 10.1016/j.ceramint.2013.03.01
- [53] F.L. Patterson. *Phys. Rev.* **56**, 10, 978 (1939).
- [55] E.C. Stoner, E. Wohlfarth. *Phil. Trans. Royal Soc. London ser. A, Math. Phys. Sci.* **240**, 599 (1948). <https://doi.org/10.1098/rsta.1948.0007>
- [55] M.A. Chuev. *ZhETF* **141**, 4, 698 (2012) (in Russian).
- [56] *Magnetic Properties of Fine Particles* / Eds J.L. Dormann, D. Fiorani. Elsevier Sci. Ltd. Series. North-Holland Delta (2012). 430 p.
- [57] S.W. da Silva, F. Nakagomi, M.S. Silva, A. Franco Jr, V.K. Garg, A.C. Oliveira, P.C. Morais. *J. Nanopart. Res.* **14**, 4, 798 (2012). DOI: 10.1007/s11051-012-0798-4
- [58] S. Ferrari, J.C. Apesteguy, F.D. Saccone. *IEEE Trans. Magn.* **51**, 6, 2900206 (2015).
- [59] C.E. Johnson, J.A. Johnson, H.Y. Hah, M. Cole, S. Gray, V. Kolesnichenko, P. Kucheryavy, G. Goloverda. *Hyperfine Interact.* **237**, 27 (2016). <https://doi.org/10.1007/s10751-016-1277-6>
- [60] M. Srivastava, S.K. Alla, Sher Singh Meena, N. Gupta, R.K. Mandal, N.K. Prasad. *New J. Chem.* **42**, 9, 7144 (2018).
- [61] P. Masina, T. Moyo, H.M.I. Abdallah. *J. Magn. Magn. Mater.* **381**, 41 (2015).
- [62] F. van der Woude, G.A. Sawatzky. *Phys. Rev. B* **4**, 9, 3159 (1971).
- [63] L.T. Kuhn, A. Bojesen, L. Timmermann, M. Meedom Nielsen, S. Morup. *J. Phys.: Condens. Matter* **14**, 49, 13551 (2002).
- [64] S. Morup, J.A. Dumesic, H. Topsee. In: *Applications of Mössbauer Spectroscopy* / Ed. R.L. Cohen. Academic Press, N.Y. (1980). V. II. P. 1–53.
- [65] S. Mørup, E. Brok, C. Frandsen. *J. Nanomater.* 720629 (2013).
- [66] A.S. Kamzin. *ZhETF* **116**, 5, 1648 (1999) (in Russian).
- [67] S.B. Singh, Ch. Srinivas, B.V. Tirupanyam, C.L. Prajapat, M.R. Singh, S.S. Meena, Pramod Bhatt, S.M. Yusuf, D.L. Sastri. *Ceram. Int.* **42**, 19188 (2016). <http://dx.doi.org/10.1016/j.ceramint.2016.09.081>
- [68] G.A. Sawatzky, F. Van Der Woude, A.H. Morrish. *J. Appl. Phys.* **39**, 2, 1204 (1968).
- [69] G.A. Sawatzky, F. Van Der Woude, A.H. Morrish. *Phys. Rev.* **187**, 2, 747 (1969).
- [70] E. Lima, A.L. Brandl, A.D. Arelaro, G.F. Goya. *J. Appl. Phys.* **99**, 8, 083908 (2006).
- [71] J.M.D. Coey. *Phys. Rev. Lett.* **27**, 17, 1140 (1971).
- [72] J. Tuček, R. Zboril, D. Petridis. *J. Nanosci. Nanotechnol.* **6**, 4, 926 (2006).
- [73] M. Eibschüts, S. Shtrikman. *J. Appl. Phys.* **39**, 2, 997 (1968).
- [74] R.H. Lindquist, G. Constabaris, W. Kündig, A.M. Portis. *J. Appl. Phys.* **39**, 2, 1001 (1968).
- [75] S. Mørup, F. Bødker, P.V. Hendriksen, S. Linderoth. *Phys. Rev. B* **52**, 1, 287 (1995).
- [76] M.A. Polikarpov, V.M. Cherepanov, M.A. Chuev, S.Yu. Shishkov, S.S. Yakimov. *J. Phys.: Conf. Ser.* **217**, 1, 012115 (2010). doi: 10.1088/1742-6596/217/1/012115
- [77] S. Mørup, C.A. Oxborrow, P.V. Hendriksen, M.S. Pedersen, M. Hanson, C. Johansson. *J. Magn. Magn. Mater.* **140–144**, Part 1, 409 (1995).